Octahedral spinel electrocatalysts for alkaline fuel cells

Yao Yang[a], Yin Xiong[a], Megan E. Holtz[b], Xinran Feng[a,c], Rui Zeng[a], Gary Chen[d], Francis J. DiSalvo[a], David A. Muller[b,e], and Héctor D. Abruña[a,1]

[a]Department of Chemistry and Chemical Biology, Cornell University, Ithaca, NY 14853; [b]School of Applied and Engineering Physics, Cornell University, Ithaca, NY 14853; [c]Cornell High Energy Synchrotron Source, Cornell University, Ithaca, NY 14853; [d]Department of Materials Science and Engineering, Cornell University, Ithaca, NY 14853; and [e]Kavli Institute at Cornell for Nanoscale Science, Cornell University, Ithaca, NY 14853

Edited by Alexis T. Bell, University of California, Berkeley, CA, and approved October 21, 2019 (received for review April 16, 2019)

Designing high-performance nonprecious electrocatalysts to replace Pt for the oxygen reduction reaction (ORR) has been a key challenge for advancing fuel cell technologies. Here, we report a systematic study of 15 different AB_2O_4/C spinel nanoparticles with well-controlled octahedral morphology. The 3 most active ORR electrocatalysts were $MnCo_2O_4$/C, $CoMn_2O_4$/C, and $CoFe_2O_4$/C. $CoMn_2O_4$/C exhibited a half-wave potential of 0.89 V in 1 M KOH, equal to the benchmark activity of Pt/C, which was ascribed to charge transfer between Co and Mn, as evidenced by X-ray absorption spectroscopy. Scanning transmission electron microscopy (STEM) provided atomic-scale, spatially resolved images, and high-energy-resolution electron-loss near-edge structure (ELNES) enabled fingerprinting the local chemical environment around the active sites. The most active $MnCo_2O_4$/C was shown to have a unique Co-Mn core–shell structure. ELNES spectra indicate that the Co in the core is predominantly $Co^{2.7+}$ while in the shell, it is mainly Co^{2+}. Broader Mn ELNES spectra indicate less-ordered nearest oxygen neighbors. Co in the shell occupies mainly tetrahedral sites, which are likely candidates as the active sites for the ORR. Such microscopic-level investigation probes the heterogeneous electronic structure at the single-nanoparticle level, and may provide a more rational basis for the design of electrocatalysts for alkaline fuel cells.

alkaline fuel cells | oxygen reduction reaction | spinel oxides | scanning transmission electron microscopy | electron energy-loss spectroscopy

As high-efficiency energy-conversion devices, proton exchange membrane fuel cells (PEMFCs) have been recognized as a crucial technology for powering electric vehicles (1–4). However, PEMFCs rely on increasing the amount of expensive Pt-based electrocatalysts to facilitate the sluggish oxygen reduction reaction (ORR) at the cathode. The catalyst cost is projected to be the largest single component (up to 40%) of the total cost of a PEMFC (5). Numerous past studies have been devoted to designing Pt-based alloy catalysts to partially replace the Pt with less-expensive metals (6–9). However, the US Department of Energy target for total Pt loading of ∼0.1 g_{Pt}/kW has yet to be achieved (10). As an alternative, anion exchange membrane fuel cells (AEMFCs) have drawn increasing attention, because they enable the use of nonprecious metal electrocatalysts, which are stable in alkaline media (11, 12). To facilitate the ORR kinetics in alkaline media, research efforts have been devoted to searching for electrocatalysts, including precious-metal–based alloys (13, 14), nitrogen-doped carbons (15–17), perovskites (18), and transition-metal oxides (19). Due to their high activity, long-term durability, and low cost, 3d transition-metal oxides with the spinel structure are a novel family of ORR electrocatalysts in alkaline fuel cells.

For the ORR and oxygen evolution reaction (OER) in alkaline media, 3d metal oxides have been intensively studied as electrocatalysts. Cobalt oxides and manganese oxides have been reported to be effective electrocatalysts for the ORR (20, 21). Furthermore, Co-based bimetallic oxides have been reported to exhibit enhanced activities for the ORR in alkaline media (22–30). Despite numerous studies of 3d metal oxide electrocatalysts, the electrocatalytic mechanism remains poorly understood (13, 19). One of the larger challenges is that their ORR activities depend on the synthetic methods employed by different research groups, and therefore different particle sizes, morphology as well as surface and crystal structures of the nanoscale electrocatalysts. These factors are formidable to control simultaneously and complicate the understanding of the intrinsic activities of these electrocatalysts. In this work, we prepared a family of 15 different AB_2O_4 spinels as ORR electrocatalysts with well-controlled particle size and morphology. We systematically investigated their ORR activity and selectivity and established correlations with the structure and local chemical environment, using macroscopic-level X-ray absorption spectroscopy (XAS) and microscopic-level scanning transmission electron microscopy (STEM) equipped with electron energy-loss spectroscopy (EELS).

Results and Discussion

A family of 15 different spinel metal oxides, AB_2O_4, (A: Mn, Fe, Co, Ni, and Cu, and B: Mn, Fe, and Co), were synthesized using a facile hydrothermal method (*SI Appendix*, Fig. S1). Briefly, 1 or 2 metal precursors were dissolved in water and reacted with ammonium hydroxide to form coordination compounds with NH_3 ligands (*SI Appendix*, Fig. S2). Monometallic or bimetallic hydroxides gradually precipitated from the solution through aging processes, at controlled temperatures, with selected solvents. The metal hydroxides subsequently formed metal-oxide nanoparticles, supported on high-surface-area carbon Ketjen black (HSC KB) with a mass loading of 40%, upon reaction in an autoclave at a mild temperature (150 °C) under a modest pressure of about 30 bar. Using powder X-ray diffraction (XRD), the resulting

Significance

We present a systematic study of a family of 15 types of octahedral spinel electrocatalysts for the oxygen reduction reaction (ORR) in alkaline fuel cells. Three specific candidates, $MnCo_2O_4$/C, $CoMn_2O_4$/C, and $CoFe_2O_4$/C, exhibited very promising ORR activity. In particular, $CoMn_2O_4$/C could rival the ORR activity and selectivity of Pt/C. Such performance was ascribed to a partial charge transfer between Co and Mn. The most active, $MnCo_2O_4$/C, exhibited a unique Co–Mn core–shell structure with heterogeneous valence states, which were probed at the single-nanoparticle level using scanning transmission and high-energy-resolution electron-loss near-edge structure. We believe that our approach, of combining advanced electron microscopy and spectroscopy, will enable the design of highly active nanocatalysts with unprecedented atomic-scale precision.

Author contributions: Y.Y., F.J.D., D.A.M., and H.D.A. designed research; Y.Y., Y.X., M.E.H., X.F., R.Z., and G.C. performed research; Y.Y. analyzed data; and Y.Y. and H.D.A. wrote the paper.

The authors declare no competing interest.

This article is a PNAS Direct Submission.

Published under the PNAS license.

[1]To whom correspondence may be addressed. Email: hda1@cornell.edu.

This article contains supporting information online at www.pnas.org/lookup/suppl/doi:10.1073/pnas.1906570116/-/DCSupplemental.

Downloaded at Cornell University Library on November 21, 2019

products were found to be single-phase spinels (*SI Appendix*, Fig. S3). The Co-based spinel family (ACo_2O_4) has a regular cubic spinel structure in which the A atoms occupy the tetrahedral sites while Co atoms occupy the octahedral sites (*SI Appendix*, Fig. S4). ACo_2O_4/C (A = Mn, Fe, Ni, and Cu) exhibited similar XRD patterns as Co_3O_4/C, with (311) as the strongest peak (*SI Appendix*, Fig. S3*A*). The XRD patterns indicated that they all adopt the cubic spinel structure. XRD patterns of $MnCo_2O_4$/C and $FeCo_2O_4$/C exhibited a slight shift of the (311) reflections to lower angles, relative to Co_3O_4/C, which is likely due to the lattice expansion upon replacing Co with Fe or Mn, as expected from the larger cationic radii of Mn and Fe relative to Co (31). In contrast to Co_3O_4, the Mn-based spinel family (AMn_2O_4) had a tetragonal spinel structure (*SI Appendix*, Fig. S3*B*), due to the Jahn–Teller distortion (32). The XRD patterns of AMn_2O_4/C exhibited more diffraction peaks at around 30° and 60°, when compared to ACo_2O_4/C, indicating a decrease in crystal symmetry (*SI Appendix*, Fig. S3*B*). The XRD patterns of the Fe-based spinel family, (AFe_2O_4/C), on the other hand, adopt a cubic inverse spinel structure, where all of the A atoms and half of the Fe atoms occupy octahedral sites, while the other half of the Fe atoms occupy the tetrahedral sites. The XRD patterns of AFe_2O_4/C (A = Mn, Co, Ni, and Cu) suggest a cubic spinel structure, similar to that of Fe_3O_4/C (*SI Appendix*, Fig. S3*C*). When compared to Fe_3O_4/C, AFe_2O_4/C exhibited intriguing peak shifts of the (311) reflections: a shift to 2θ values in the case of $MnFe_2O_4$/C and a shift to higher 2θ values for $CoFe_2O_4$/C, $NiFe_2O_4$/C, and $CuFe_2O_4$/C. These observations likely originate from the fact that relative to Fe, Mn has a larger atomic radius while Co, Ni, and Cu have smaller radii, causing lattice expansions and contractions, respectively. Average domain sizes of AB_2O_4/C nanoparticles were analyzed using the Scherrer equation (*SI Appendix*, Table S1).

With the crystal structures of AB_2O_4/C confirmed by XRD, the ORR activities of AB_2O_4/C were preliminarily evaluated using the rotating-disk electrode (RDE) technique. The ORR polarization profile for Pt/C exhibited a half-wave potential ($E_{1/2}$) of 0.890 V vs. the reversible hydrogen electrode (RHE), a benchmark activity value for Pt in 1 M KOH (dashed lines in Fig. 1 *A*–*C*). The ORR polarization profiles of ACo_2O_4/C in Fig. 1*A* suggest that ACo_2O_4/C reaches a transport limited current, I_d, close to that of Pt/C, indicating that the main reaction product is water, as is the case on Pt. It should be noted that, based on the Levich equation, the I_d for the $4e^-$ reduction of oxygen in 0.1 M oxygen-saturated KOH or $HClO_4$ should be −5.5 mA/cm^2 at 1,600 rpm. Since the O_2 solubility in 1 M KOH (as used in the present work) at 25 °C and 1 atm is 8.42×10^{-4} mol/L, which is 70% of its value in 0.1 M KOH (1.21×10^{-3} mol/L) (33), the I_d for the $4e^-$ reduction of oxygen in 1 M KOH will be correspondingly lower with a value of −3.8 mA/cm^2 at 1,600 rpm. The ORR profiles of ACo_2O_4/C were magnified in *SI Appendix*, Fig. S5*A* to better illustrate the difference in the early kinetic-controlled region (0.85 to 1.0 V). $E_{1/2}$, onset potential (E_{onset}), and I_d values are summarized in *SI Appendix*, Table S2 for better quantitative and comparative assessment. Among the 5 types of ACo_2O_4/C catalysts, $MnCo_2O_4$/C clearly stands out as the most active candidate in the Co-based spinel family with an $E_{1/2}$ value of 0.855 V vs. RHE. The mass-specific activity (MA) at 0.85 V was employed as a metric value to partially evaluate the initial electrocatalytic activity. As shown in Fig. 1*D*, the MA at 0.85 V of $MnCo_2O_4$ (43 A/g) was about 1.5× as high as that of monometallic Co_3O_4/C (27 A/g), and over 2×, relative to ACo_2O_4/C (A = Fe, Ni, and Cu), respectively. For the Mn-based spinel family, ORR polarization profiles of AMn_2O_4/C demonstrate that $CoMn_2O_4$/C has significant ORR activity with an $E_{1/2}$ value of 0.844 V, when compared to that of the monometallic Mn_3O_4/C (black curve). However, the AMn_2O_4/C materials involving Fe, Ni, and Cu exhibited a decrease in activity (Fig. 1*B*). The MA at 0.85 V of $CoMn_2O_4$/C (31 A/g) was 2.5× as high as that of

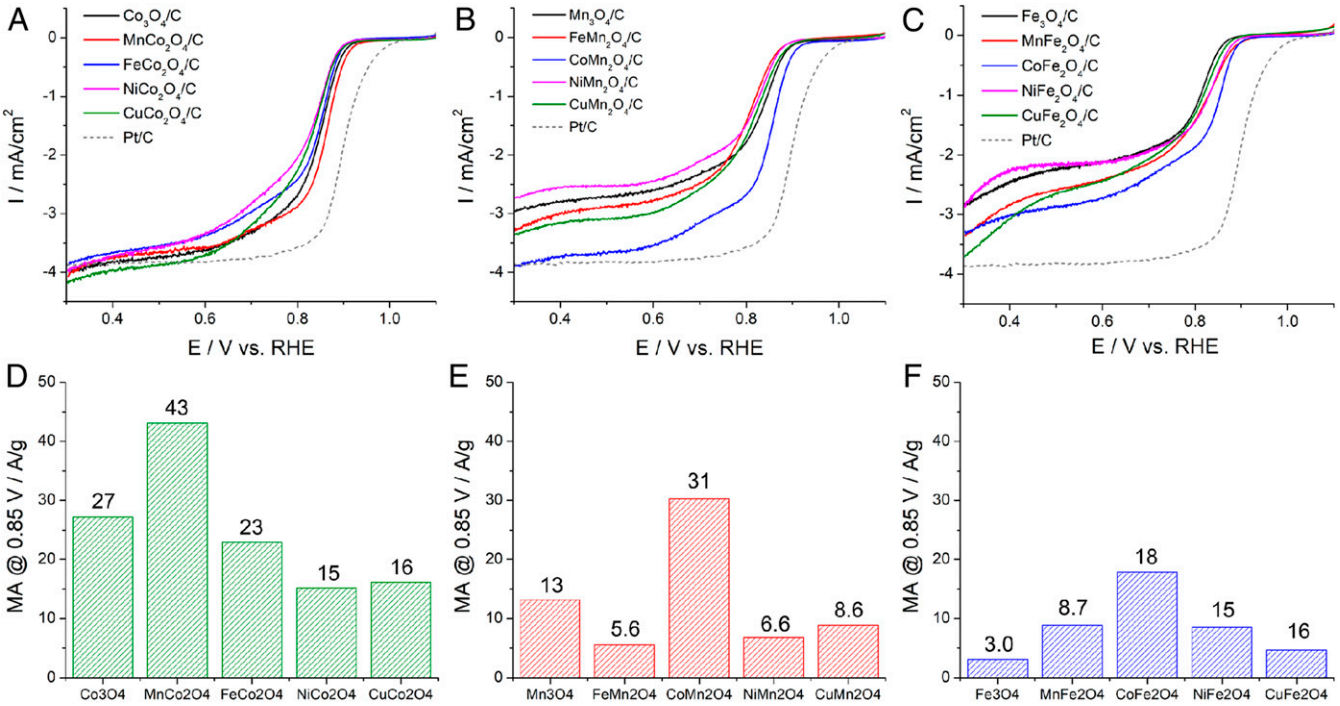

Fig. 1. ORR activity of AB_2O_4/C spinel electrocatalysts. (*A*–*C*) ORR polarization profiles of 15 different AB_2O_4/C in O_2-saturated 1 M KOH at 1,600 rpm and a scan rate of 5 mV/s. Mass loading of metal oxides and Pt: 0.1 mg/cm^2 and 25 μg/cm^2, respectively. (*D*–*F*) MA of AB_2O_4/C at 0.85 V vs. RHE, which was calculated by normalizing the kinetic current to the mass loading of the metal oxide. $MnCo_2O_4$/C, $CoMn_2O_4$/C, and $CoFe_2O_4$/C were found to be the 3 most active ORR electrocatalysts.

Downloaded at Cornell University Library on November 21, 2019

monometallic Mn_3O_4/C (13 A/g), and over 3× higher than other AMn_2O_4/C involving Fe, Ni, and Cu (Fig. 1*E*). Finally, the ORR polarization profiles of the Fe-based spinel family, AFe_2O_4/C, exhibited an overall lower activity, relative to the Co-based and Mn-based spinel families. I_d values of AFe_2O_4/C were noticeably lower than that of Pt/C, indicating that a significant amount of peroxide formed (Fig. 1*C*). Among the Fe-based spinels, the most active, $CoFe_2O_4$/C, had an MA value (18 A/g) twice as large as those of $MnFe_2O_4$/C (8.7 A/g) and $NiFe_2O_4$/C (8.7 A/g) and over a 4-fold increase, relative to Fe_3O_4/C and $CuFe_2O_4$/C (Fig. 1*F*).

In summary, $MnCo_2O_4$/C, $CoMn_2O_4$/C, and $CoFe_2O_4$/C have been demonstrated to be the 3 most active candidates among the 15 types of AB_2O_4/C spinels. The impact of particle sizes and types of carbon substrate are discussed in detail in *SI Appendix*, Figs. S6 and S7. Cyclic voltammetric (CV) profiles of mono/bimetallic oxides were compared to reveal more information about the active redox couples for catalyzing the ORR (*SI Appendix*, Fig. S8). Among those, $MnCo_2O_4$/C exhibited a larger redox current than $CoMn_2O_4$/C and $CoFe_2O_4$/C, and a pronounced minor redox couple at 1.05/1.04 V. Detailed analysis of the CV profiles suggests that this minor redox couple comes from monolayer species on the surface with a highly reversible reaction process (*SI Appendix*, Fig. S9), which may partially explain the highest initial activity of $MnCo_2O_4$ among all AB_2O_4/C materials. $MnCo_2O_4$/C and $CoMn_2O_4$/C exhibited smaller Tafel slopes of 46 and 49 mV/dec, respectively, relative to Pt/C (66 mV/dec), suggesting a smaller overpotential to achieve the same kinetic current change (*SI Appendix*, Fig. S10).

After studying the ORR activity of AB_2O_4/C and corresponding redox couples, the catalyst selectivity was further investigated using the rotating ring-disk electrode (RRDE) technique. The ORR selectivity (H_2O vs. H_2O_2) of Pt/C was first examined using a glassy carbon (GC)-disk and Pt-ring RRDE, with the ring potential held at 1.3 V vs. RHE to oxidize any peroxide generated at the GC disk (34). As shown in *SI Appendix*, Fig. S11, Pt/C exhibits a potential-dependent H_2O_2 yield of 2∼5% and an electron transfer number of 3.98 to 3.90. RRDE profiles of $CoMn_2O_4$/C exhibited a peak ring current of ∼35 μA, larger than that of Pt/C (∼8 μA), indicating a larger fraction of peroxide formation. H_2O_2 yield and electron transfer number were calculated to be around 20% and 3.6, respectively. Inspired by previous studies on the impact of loading of Fe-*N*-C catalysts on H_2O_2 formation (35–38), RRDE profiles of $CoMn_2O_4$/C at various loadings were measured. When the metal-oxide loading was increased from 0.1 to 0.5 mg/cm^2, a significant improvement in ORR activity was observed with the $E_{1/2}$ shifting positively by 30 mV from 0.86 V at 0.1 mg/cm^2 to 0.89 V at 0.5 mg/cm^2. This last value is essentially the same as the measured benchmark value of Pt/C (0.89 V) (Fig. 2*A*). The ring current dropped noticeably at higher loadings and the H_2O_2 yield at 0.9 V decreased from 18% at 0.1 mg/cm^2 to 12.5% at 0.25 mg/cm^2, and finally to as low as 5% at 0.5 mg/cm^2 (Fig. 2 *B* and *C*). The electron transfer number at 0.9 V increased from 3.65 at 0.1 mg/cm^2 to as high as 3.9 at 0.5 mg/cm^2 (Fig. 2*D*). A similar improvement was also observed for $MnCo_2O_4$/C (*SI Appendix*, Fig. S12). The peroxide yield of Co–Mn oxides in alkaline media was comparable to previous reports on similar catalysts (39). At an ultrahigh loading level of 1.0 $mg_{metal\ oxide}$/cm^2, the ORR polarization profile of $CoMn_2O_4$ in the mass-transport-controlled region (E < 0.8 V) no longer followed the typical diffusion-limited characteristic, indicating significant mass-transport limitations arising from the very thick catalyst layer. Therefore, we propose that metal oxides, at higher loading, can provide a higher number of active sites and a sufficiently thick catalyst layer to decompose a significant portion of the electrogenerated H_2O_2 before it escapes from the catalyst layer into solution. The high loadings of Co–Mn oxides are critical in practical membrane–electrode assembly measurements for a high peak power density of > 1 W/cm^2 (*SI Appendix*, Fig. S13), as we reported, in detail, in our recent work (25, 26).

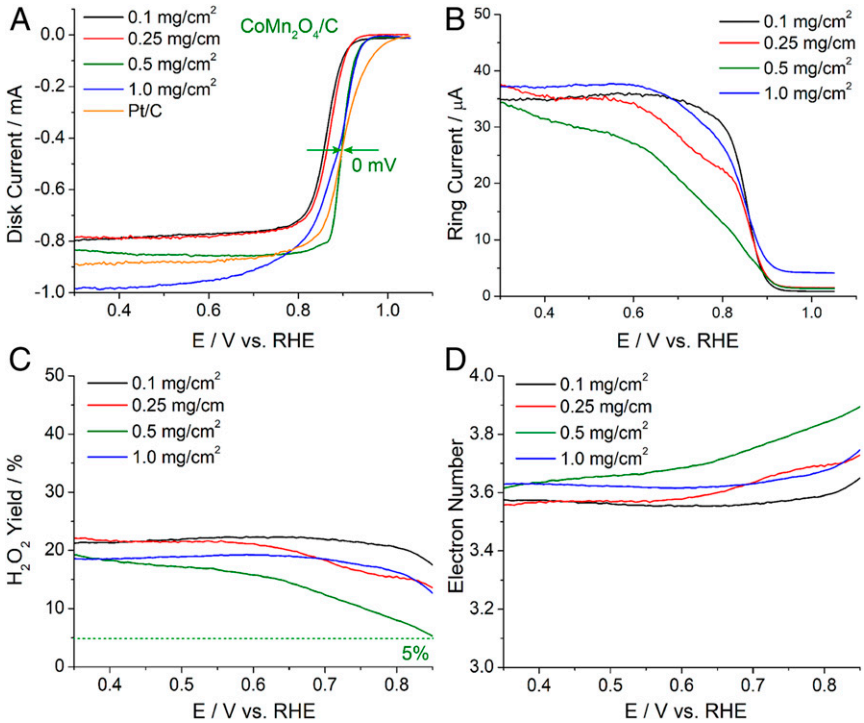

Fig. 2. ORR selectivity of $CoMn_2O_4$/C at various mass loadings of metal oxides. (*A* and *B*) RRDE profiles of disk and ring currents measured on a GC-disk and Pt-ring RRDE in O_2-saturated 1 M KOH at 1,600 rpm and a scan rate of 5 mV/s. Ring potential was held at 1.3 V vs. RHE to oxidize the H_2O_2 electrogenerated at the disk. (*C* and *D*) H_2O_2 yields and electron numbers calculated based on ring and disk currents. $CoMn_2O_4$/C at an optimal loading of 0.5 mg/cm^2 achieved an $E_{1/2}$ value of 0.89 V, equal to the benchmark Pt/C, and a H_2O_2 yield of 5% at 0.85 V, comparable to Pt/C.

Downloaded at Cornell University Library on November 21, 2019

In order to establish why $MnCo_2O_4$/C, $CoMn_2O_4$/C, and $CoFe_2O_4$ stand out as the 3 most active electrocatalysts toward the ORR, thorough investigations of the morphology, crystal structure, and local chemical environment were carried out employing macroscopic-level XAS and microscopic-level STEM-EELS. The X-ray absorption near-edge structure (XANES) of Mn in Fig. 3*A* indicate that gradually increasing the Co contents in Mn-based spinels, from Mn_3O_4/C to $CoMn_2O_4$/C and $MnCo_2O_4$/C, leads to a progressive positive shift of the Mn-edge energy, indicating a higher Mn valence state and charge transfer from Mn to Co. Symmetrically, a gradual increase in the Mn contents in Co-based spinels, from Co_3O_4/C to $MnCo_2O_4$/C and $CoMn_2O_4$/C, results in a negative shift in the Co-edge energy, again suggesting a lower Co valence state and charge transfer from Mn to Co (Fig. 3*B*). This local interaction indicates that Mn and Co have mutually altered their electronic structures, which may explain the fact that both $MnCo_2O_4$/C and $CoMn_2O_4$/C exhibit significantly enhanced ORR activity, relative to their monometallic oxide counterparts, Mn_3O_4/C and Co_3O_4/C, respectively. XANES spectra of Fe-based spinels are discussed in *SI Appendix*, Fig. S14.

The morphology and microstructure of $MnCo_2O_4$/C and $CoMn_2O_4$ were examined using an aberration-corrected STEM. Fig. 4 *A* and *B* exhibit the well-defined octahedral morphology of $MnCo_2O_4$ nanoparticles. The STEM image intensity varies at different regions of the $MnCo_2O_4$ nanoparticles (Fig. 4*A* and *SI Appendix*, Fig. S15), indicating the possible existence of nanometer-scale pores or channels on the surface or inside the metal oxide nanoparticle, which may expose the inner part of the metal oxide to O_2 molecules (39–41). The particle size distribution histogram of ~200 $MnCo_2O_4$ nanoparticles indicates an average particle size of 35 nm (*SI Appendix*, Fig. S16). The majority of the $MnCo_2O_4$ nanoparticles appear to have multiple subdomains since the domain size, calculated from XRD, was 15 nm. $CoMn_2O_4$/C nanoparticles were found to have similar octahedral morphology and multiple subdomains (*SI Appendix*, Fig. S17). Furthermore, atomic-scale high-angle annular dark-field (HAADF)-STEM images of $MnCo_2O_4$ clearly show the spinel structure on the [110] zone axis (Fig. 4*C* and *SI Appendix*, Fig. S18 *A* and *B*). $MnCo_2O_4$ exhibits hexagonal repeating unit cells, as indicated by the dashed boxes with 2 d-spacings of 3.6 and 2.1 Å (Fig. 4*C*), which match well with the theoretical values (3.64 and 2.12 Å), based on the crystal model of $MnCo_2O_4$ (powder diffraction file [PDF] 01–084-0482). The atomic columns, labeled **b** and **c**, on the side of the $MnCo_2O_4$ unit cell in Fig. 4*C*, show a lower intensity than that of atomic columns, labeled **a**, at the center. The intensity variation comes from the fact that atomic columns, **a**, have a higher atom density than those of **b** and **c**, based on the tilted [110] zone axis (Fig. 4*E*). Atomic-scale STEM images of $CoMn_2O_4$ exhibit the characteristic layered structure on the $[01\bar{1}]$ zone axis of a tetragonal spinel (Fig. 4*F* and *SI Appendix*, Fig. S18 *C* and *D*). Two d-spacings of 4.9 and 3.0 Å, which were perpendicular to each other, matched well with the theoretical values (4.88 and 3.04 Å), respectively, based on the crystal model of $CoMn_2O_4$ (PDF 01–077-0471) (Fig. 4 *F* and *G*). Atomic-scale electron EELS of the Mn L_2 edge provides evidence of the layered structure on the $[01\bar{1}]$ zone axis (Fig. 4 *F*, *Inset*). It is of particular interest to observe, in Fig. 4*F*, that atomic columns, **b**, on the side, show a lower intensity than atomic columns, **a**, at the corner. This image intensity variation also originates from the fact that atomic columns, **b**, exhibit a lower atom density than atomic columns, **a**, based on the tilted $[01\bar{1}]$ zone axis in Fig. 4*H*. A similar layered structure was also observed for $MnCo_2O_4$ though at a different $[11\bar{2}]$ zone axis (*SI Appendix*, Fig. S19).

The chemical composition of selected metal oxides was then investigated using EELS. EELS elemental maps were extracted from the sharp Mn, Co, and Fe L_3 edges of the core-loss EELS spectra (*SI Appendix*, Fig. S20). Fig. 5 *A–C* present an octahedral $MnCo_2O_4$ nanoparticle with the corresponding EELS elemental maps of Mn (red) and Co (green). The composite map of Mn vs. Co of $MnCo_2O_4$ exhibits a core–shell structure with 2 to 4-nm Mn shell on the surface (Fig. 5*D*). We observed that $CoMn_2O_4$/C (Fig. 5 *E–H*) and $CoFe_2O_4$/C (Fig. 5 *I–L*) have a relatively homogeneous elemental distribution of Co vs. Mn and Co vs. Fe, respectively. Atomic-scale STEM-EELS of $MnCo_2O_4$ suggests smooth elemental gradients from a Co-rich core to an Mn-rich shell without a distinct boundary (*SI Appendix*, Fig. S21). This helps corroborate the previous CV analysis of the minor redox couple of $MnCo_2O_4$/C (*SI Appendix*, Fig. S9), as the STEM-EELS mapping of $MnCo_2O_4$ further suggests that the monolayer species on the surface is Mn-rich, which may serve as a key structural factor for the pronounced ORR activity of $MnCo_2O_4$.

To gain a detailed description of the local electronic structure of $MnCo_2O_4$/C, we performed fine-structure EELS investigations with high spatial resolution. We employed the energy-loss near-edge structure (ELNES) that reflects the density of unfilled states (unfilled DOS) above the Fermi level (E_F), which is particularly sensitive to the local atomic environment, such as valence state, chemical bonding, and coordination (predominantly nearest-neighbor) (42). Measurements of the fine structure can help us understand the electronic structure of the catalysts and ultimately establish its correlation with electrocatalytic performance. Normally 3d transitional metals have sharp L edges in core-loss spectra (*SI Appendix*, Fig. S20), which can be further divided into an L_2 edge ($2p^{1/2}$ to $3d^{3/2}$ transition) and a stronger L_3 edge ($2p^{3/2}$ to $3d^{3/2}3d^{5/2}$ transition). In this work, ELNES spectra

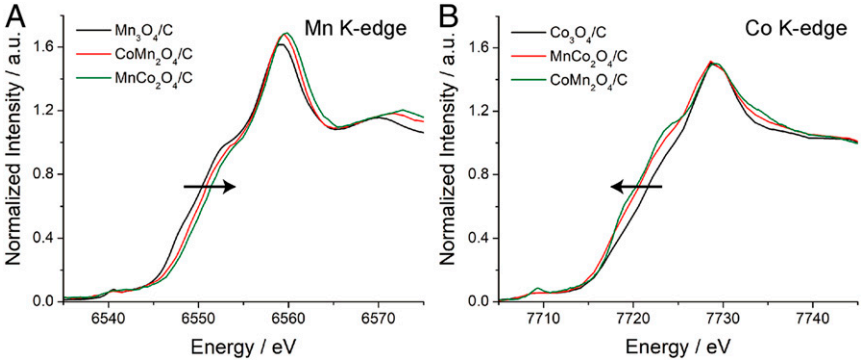

Fig. 3. Powder XANES spectra of spinel $MnCo_2O_4$/C and $CoMn_2O_4$/C. (*A* and *B*) XANES spectra of Mn and Co K edges of Mn_3O_4/C, $CoMn_2O_4$/C, $MnCo_2O_4$/C, and Co_3O_4/C, respectively. Black arrows indicate the positive and negative shifts in the edge energy of Mn and Co, respectively. The symmetrical changes in their electronic structures indicate synergistic effects between Co and Mn, which may explain the pronounced ORR activity of $MnCo_2O_4$/C and $CoMn_2O_4$/C.

Downloaded at Cornell University Library on November 21, 2019

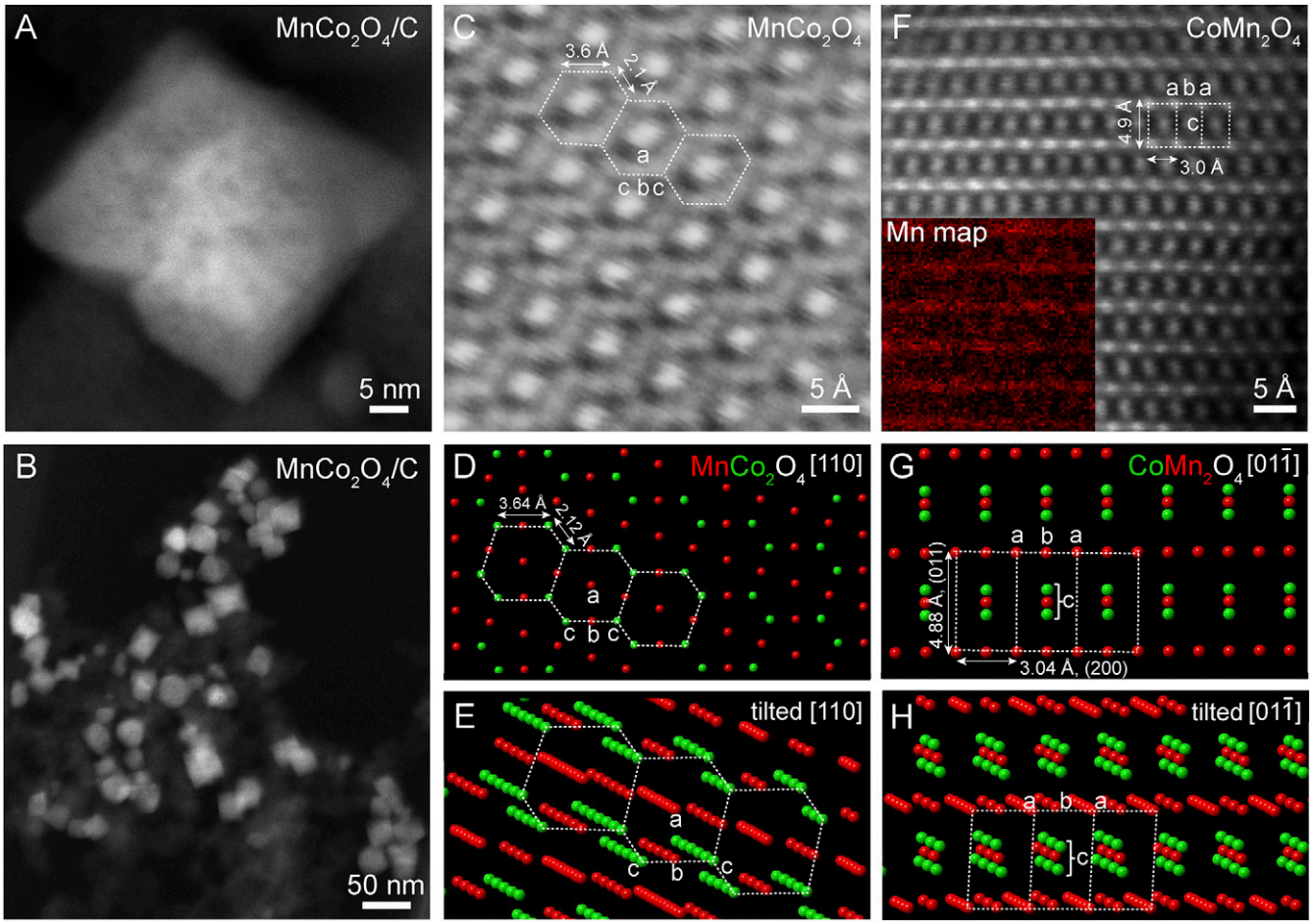

Fig. 4. HAADF-STEM images of spinel $MnCo_2O_4$/C and $CoMn_2O_4$/C. (*A* and *B*) Octahedral $MnCo_2O_4$ nanoparticles with an average particle size of 35 nm supported on HSC KB carbon. (*C–E*) Atomic-scale STEM image of $MnCo_2O_4$ and the corresponding crystal model projected on the [110] zone axis. Atom columns **a** exhibit brighter intensity than **b** and **c** due to the higher atom density, as shown in the tilted crystal model in *E*. (*F*) Atomic-scale STEM image of $CoMn_2O_4$ on the $[01\bar{1}]$ zone axis. (*Inset*) Atomic-scale EELS elemental mapping of Mn showing the characteristic layered structure in spinels. (*G* and *H*) Crystal model of $CoMn_2O_4$ corresponding to the image in *F* with 2 perpendicular lattice planes of (011) and (200). Atom columns **a** exhibit higher intensity than **b** due to the higher atom density, as shown in the tilted crystal model in *H*.

with an energy resolution of 0.5 eV (*SI Appendix*, Fig. S22) were first calibrated against the simultaneously acquired zero loss peak and then employed to fingerprint the catalyst structure.

We further investigated the core–shell structure of $MnCo_2O_4$ to see how the compositional changes across the nanoparticle affect the local binding of both Mn and Co using ELNES (Fig. 6). We first obtained reference ELNES spectra for Co and Mn in 2+, 2.67+, and 3+ valence states (*SI Appendix*, Figs. S23 and S24) using CoO (MnO), Co_3O_4 (Mn_3O_4), and CoOOH (Mn_2O_3), respectively. The edges progressively shift to higher energy values for higher valence states, due to the larger energy loss for ejecting electrons from metal p orbitals at higher metal valence states. Larger L_3 to L_2 intensity ratios at higher metal valence states also indicate more covalent metal–oxygen bonds (43). Co_3O_4 and Mn_3O_4 (II,III) appear to have ELNES spectra between +2 and +3 valence states, and the spectra can be reproduced from linear combinations of CoO, MnO (II) and CoOOH, Mn_2O_3 (III), respectively (43). Once the reference spectra were obtained, we compared them to the ELNES of the $MnCo_2O_4$ core–shell structure. Shell sections at the 4 corners were labeled as S-1, S-2, S-3, and S-4 (Fig. 6 *A* and *B*). ELNES spectra of Co and Mn L edges were processed to remove some of the noise (*SI Appendix*, Fig. S25). ELNES spectra of Co and Mn in the shell exhibited similar features among the 4 different shell locations (S-1, S-2, S-3, and S-4), suggesting that all shell sections likely have a uniform chemical bonding environment of Co (Fig. 6*E*) and Mn (*SI Appendix*, Fig. S26). The ELNES spectrum of the Co L_3 edge in the core resembles the features of Co_3O_4 (II,III), indicating Co in the core is predominantly cubic spinel, and Co^{2+} in the core occupies the tetrahedral sites while Co^{3+} in the core occupies half of the octahedral sites (Fig. 6*C*). In contrast, Co in the shell appears (convincingly) to be Co^{2+}, resembling the feature of the CoO (II) reference (Fig. 6*C*). Furthermore, ELNES spectra of the Mn L_3 edge indicate that Mn in the core has a larger contribution from higher Mn valence, when compared to Mn in the shell (Fig. 6*D*). Mn L_3 edges, at both core and shell, are much broader than the Mn oxide references, indicating a less-ordered nearest-neighbor oxygen coordination environment, and a lower crystal symmetry, likely caused by a Jahn–Teller distortion of $Mn^{3+}[3d^4]$ (44). In summary, both Co and Mn have lower metal valences in the shell, suggesting that the shell may have more oxygen vacancies. Compared with the core, where Co occupies both tetrahedral and octahedral sites, Co in the shell prefers to stay in the tetrahedral sites as it is present mainly as Co^{2+}. As a comparison, Mn in the shell occupies both tetrahedral and octahedral sites.

Besides the metal L edges, the oxygen K edge can also provide valuable complementary information about the chemical bonding

Downloaded at Cornell University Library on November 21, 2019

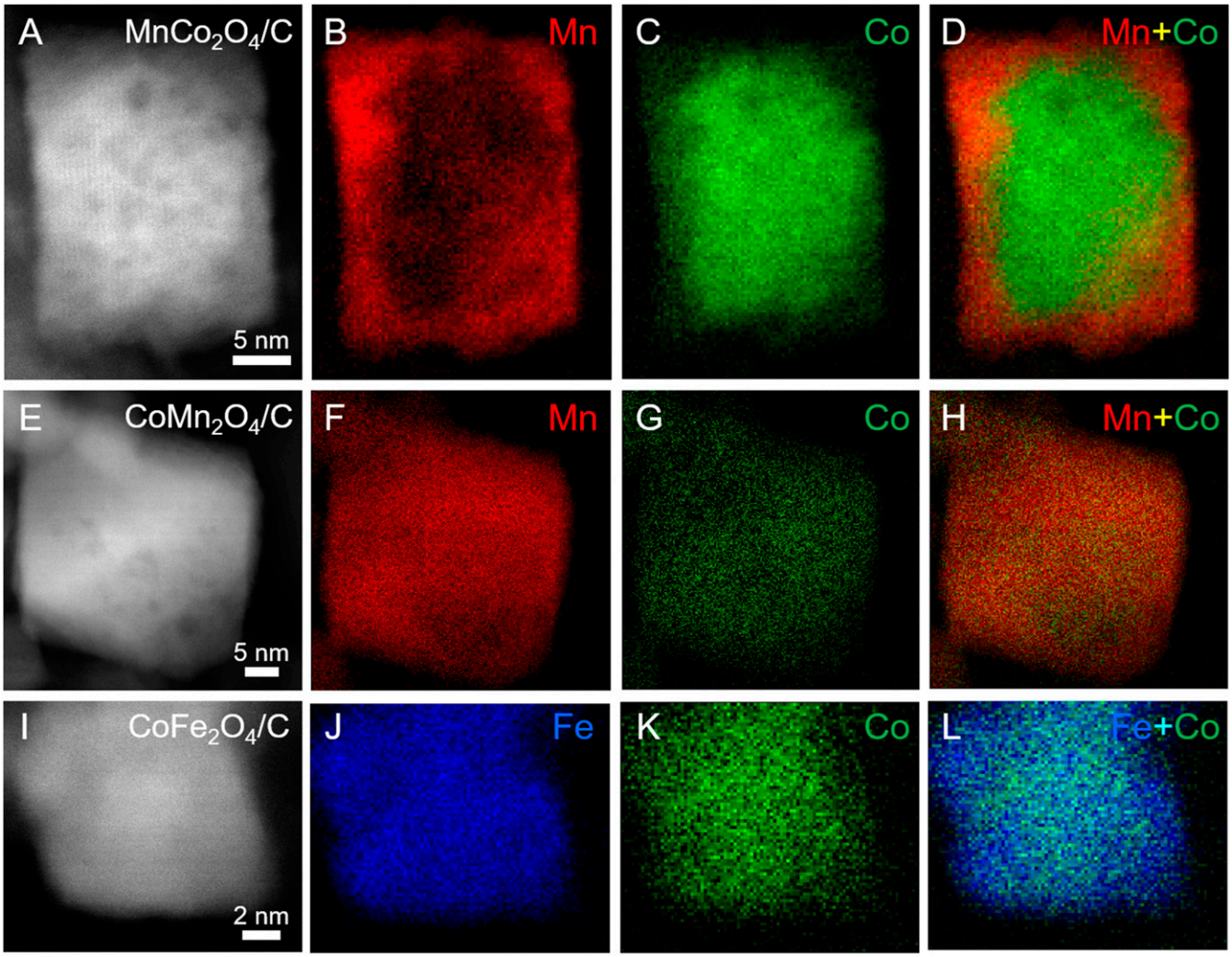

Fig. 5. EELS elemental mapping of $MnCo_2O_4$/C, $CoMn_2O_4$/C, and $CoFe_2O_4$/C. (*A–D*) STEM image of $MnCo_2O_4$/C and the corresponding EELS elemental maps of Mn and Co. Composite map in *D* exhibits a Co–Mn core–shell structure with a 2- to 4-nm Mn shell. (*E–L*) STEM images of $CoMn_2O_4$/C (*E*) and $CoFe_2O_4$ (*I*), respectively, and the corresponding EELS elemental maps of Mn–Co (*F–H*) and Fe–Co (*J–L*), respectively. Composite maps of Mn vs. Co in *H* and Fe vs. Co in *L* suggest relatively homogeneous distributions of Mn with Co and Fe with Co, respectively.

of the metal center (45). The first and second peaks in the ELNES spectra of the O K edge represent the joint density of states between the O-2p and the partially filled transition-metal 3d bands and empty 4s,p bands, respectively (Fig. 6*F*). Oxygen in the core exhibits a higher-energy second peak, relative to O in the shell, which normally indicates that the metal center in the core has a higher valence (45). This positive shift agrees with the ELNES spectra of Mn oxide references where the second peak gradually shifts to higher energies as the Mn valence increases from MnO (+2) to Mn_3O_4 (+2.67) and Mn_2O_3 (+3) (*SI Appendix*, Fig. S27*A*). Additionally, a larger first-to-second peak ratio in the core indicates that the metal center has a higher metal valence, meaning a higher DOS of unfilled 3d bands available for mixing with the O 2p bands and typically a higher metal covalency. This can also be clearly observed in the ELNES spectra of Co oxide references where CoOOH (+3) and Co_3O_4(+2.67) have larger first-to-second peak ratios than CoO (+2) (*SI Appendix*, Fig. S27*B*). The critical spectroscopic evidence of Co, Mn, and O in the core/shell was further confirmed on another $MnCo_2O_4$ nanoparticle (*SI Appendix*, Figs. S28 and S29) and examined on 5 other particles for reproducibility. In summary, the overall similarity in ELNES features of the O K edges between core and shell indicates that the core and shell likely share the same spinel structure, which is consistent with XRD as well as the STEM image of a single-crystal spinel $MnCo_2O_4$ NP (*SI Appendix*, Fig. S21).

Finally, with the intent of developing a Pt-free cathode for AEMFCs, nonprecious ORR electrocatalysts need to not only exhibit high initial ORR activity, but also achieve long-term durability (4, 5). As shown in *SI Appendix*, Fig. S30, $MnCo_2O_4$/C and $CoMn_2O_4$/C exhibited an activity decay comparable to Pt/C, in terms of the negative shift in the $E_{1/2}$. The ORR activity decrease was partially ascribed to the loss of electrochemical surface area, as evidenced by the lower redox peak current after 10,000 CV cycles. Particle aggregation of both $MnCo_2O_4$/C and $CoMn_2O_4$/C was observed from STEM images of catalysts after 10,000 cycles (*SI Appendix*, Figs. S31 and S32), which was consistent with the surface area loss in CV profiles. Interestingly, from the energy dispersive X-ray (EDX) spectroscopy quantitative analysis, the relative contents of Mn and Co were virtually the same before and after CV cycles, indicating a relatively stable elemental distribution through long-term cycling (*SI Appendix*, Fig. S33). Furthermore, EELS maps of catalysts after durability testing suggest that $MnCo_2O_4$/C still preserves the Co–Mn core–shell structure although with a thinner Mn shell (*SI Appendix*, Fig. S34), while $CoMn_2O_4$/C after 10,000 cycles exhibits the

Downloaded at Cornell University Library on November 21, 2019

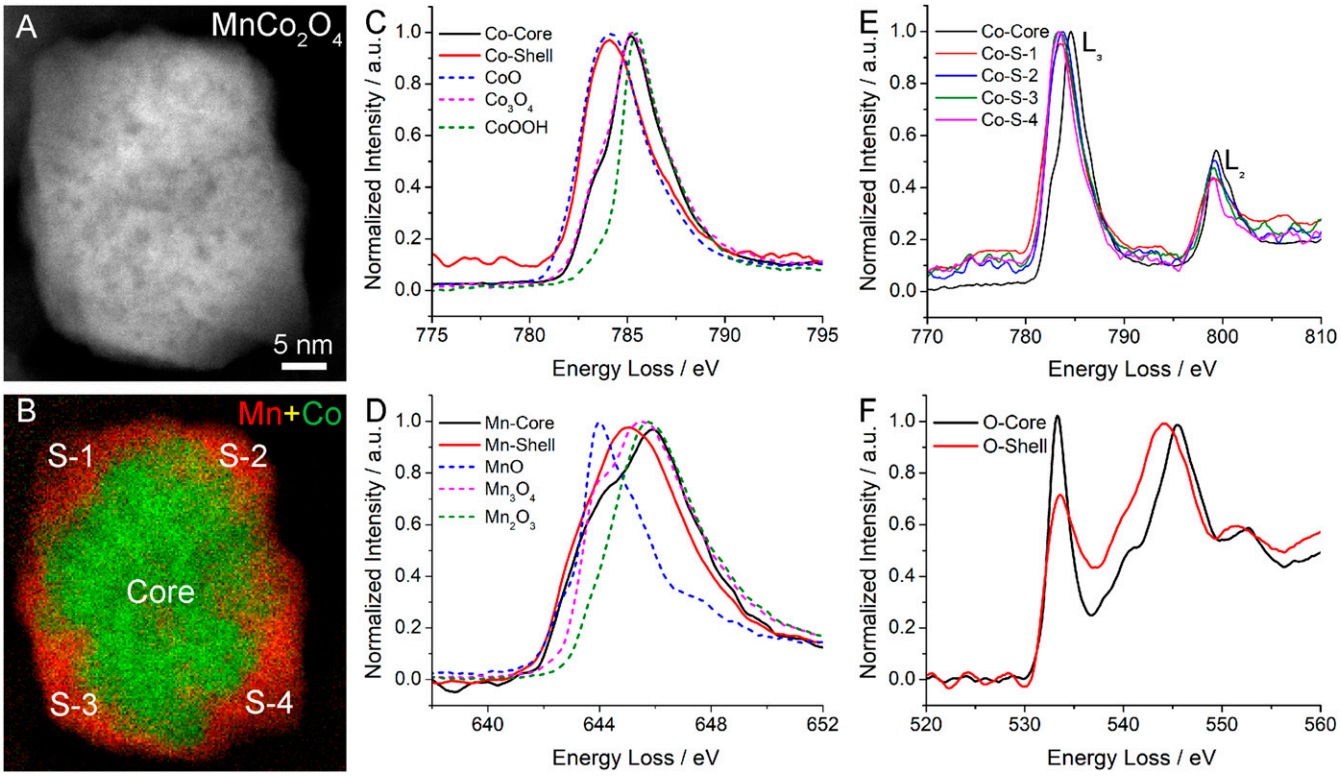

Fig. 6. ELNES of the core–shell $MnCo_2O_4$/C with an energy resolution of 0.5 eV. (*A* and *B*) STEM image and EELS elemental map of 1 $MnCo_2O_4$ nanoparticle with an Mn-rich shell. Four different regions on the shell for further analysis were labeled as S-1, S-2, S-3, and S-4, respectively. (*C*) Comparison of average ELNES spectra of Co in the core and shell with standard Co oxide references. Co at the core clearly has a major contribution from Co_3O_4 (II,III) while Co at the shell is predominantly Co^{2+}, resembling the feature of CoO (II) reference. (*D*) Comparison of average ELNES spectra of Mn in the core and shell with standard Mn oxide references. Mn ELNES spectra, with a higher valence in the core than in the shell, exhibit broader features than Co, indicating a less-ordered nearest-neighbor environment. (*E*) ELNES spectra of Co in the core and shell show the similar features of Co $L_{2,3}$ edges among S-1~4, which indicates the relatively uniform local chemical environment of Co at the shell. (*F*) ELNES average spectra of oxygen K edge in the core and shell corresponding to the nanoparticle. The higher first-to-second peak ratio of ELNES spectrum in the core indicates a higher metal valence and metal-oxygen bond covalency. Similar ELNES features of the core and shell suggests they possibly share the same spinel structure.

similar uniform distribution of Co and Mn as the initial state (*SI Appendix*, Fig. S35). The aforementioned structural investigation provides us with a microscopic picture of the catalyst evolution during durability tests.

In summary, a class of 15 compositions of AB_2O_4/C spinel electrocatalysts for the ORR has been rationally designed with a well-controlled particle size and morphology. $CoMn_2O_4$ could reach an ORR activity and selectivity (H_2O vs. H_2O_2) comparable to Pt/C. Crystal structures of electrocatalysts were thoroughly examined, using both macroscopic-level XAS and microscopic-level STEM-EELS techniques. ELNES spectra provided fine details on the local chemical environment of single $MnCo_2O_4$ nanoparticles with a unique Co–Mn core–shell structure. The methodology of using analytical electron microscopy and spectroscopy in this work can enable researchers in the broad catalyst community to understand and design electrocatalysts with atomic-scale precision. This in-depth structural investigation will offer insightful strategies for material design and developments in the renewable energy community, in general, and in fuel cells, in particular.

Methods

A class of 15 types of AB_2O_4/C, A = Mn, Fe, Co, Ni, Cu, and B = Mn, Fe, Co, has been synthesized using a facile hydrothermal method. In general, the pH and ethanol/H_2O volume ratio in the solvent controlled the precipitation rate of metal hydroxides, and therefore influenced the final metal-oxide particle size, morphology, and distribution on the carbon substrate. The crystal structures were examined by XRD and XANES at Cornell High Energy Synchrotron Source (CHESS). The microstructures and chemical compositions were investigated by STEM imaging and EELS spectroscopy (Cornell Nion UltraSTEM). The electrochemical activity and selectivity were evaluated in RDE and RRDE measurements in O_2-saturated 1 M KOH at 1,600 rpm and 5 mV/s. More experimental details can be found in *SI Appendix*.

ACKNOWLEDGMENTS. This work was primarily supported by the Center for Alkaline-Based Energy Solutions, an Energy Frontier Research Center program supported by the US Department of Energy, under Grant DE-SC0019445. This work made use of TEM facilities at the Cornell Center for Materials Research (CCMR) which are supported through the National Science Foundation Materials Research Science and Engineering Center program (DMR-1719875). We are grateful to Malcolm (Mick) Thomas at CCMR for the help in Nion UltraSTEM. This work is based upon research conducted at CHESS, which is supported by the National Science Foundation under Award DMR-1332208. Y.Y. acknowledges the generous help in matrix laboratory (MATLAB) coding from Dr. Zhen Chen and Dr. Megan Holtz in the Muller group at Cornell University. X.F. also acknowledges financial support from CHESS under the same award. We appreciate the assistance of CHESS staff scientists at C1 and F3 beamlines, Kenneth D. Finkelstein, Christopher Pollock, and Rong Huang.

1. L. Wang *et al*., Tunable intrinsic strain in two-dimensional transition metal electrocatalysts. *Science* **363**, 870–874 (2019).
2. V. R. Stamenkovic, D. Strmcnik, P. P. Lopes, N. M. Markovic, Energy and fuels from electrochemical interfaces. *Nat. Mater.* **16**, 57–69 (2016).
3. Y. Xiong *et al*., Revealing the atomic ordering of binary intermetallics using in situ heating techniques at multilength scales. *Proc. Natl. Acad. Sci. U.S.A.* **116**, 1974–1983 (2019).
4. H. A. Gasteiger, S. S. Kocha, B. Somali, F. T. Wagner, Activity benchmarks and requirements for Pt, Pt-alloy, and non-Pt oxygen reduction catalysts for PEMFCs. *Appl. Catal. B* **56**, 9–35 (2005).

Downloaded at Cornell University Library on November 21, 2019

5. D. Papageorgopoulos, "Annual merit review and peer evaluation meeting in fuel cells program area" (US Department of Energy, Washington, DC, 2017; https://www.hydrogen.energy.gov/annual_review17_report.html).
6. D. Wang *et al*., Structurally ordered intermetallic platinum-cobalt core-shell nanoparticles with enhanced activity and stability as oxygen reduction electrocatalysts. *Nat. Mater.* **12**, 81–87 (2013).
7. Y. Xiong, Y. Yang, F. J. DiSalvo, H. D. Abruña, Pt-decorated composition-tunable Pd–Fe@Pd/C core–shell nanoparticles with enhanced electrocatalytic activity toward the oxygen reduction reaction. *J. Am. Chem. Soc.* **140**, 7248–7255 (2018).
8. Y. Xiong, L. Xiao, Y. Yang, F. J. DiSalvo, H. D. Abruña, High-loading intermetallic Pt_3Co/C core–shell nanoparticles as enhanced activity electrocatalysts toward the oxygen reduction reaction (ORR). *Chem. Mater.* **30**, 1532–1539 (2018).
9. G. Wang *et al*., Pt skin on AuCu intermetallic substrate: A strategy to maximize Pt utilization for fuel cells. *J. Am. Chem. Soc.* **136**, 9643–9649 (2014).
10. O. Groger, H. A. Gasteiger, J. P. Suchsland, Review—Electromobility: Batteries or fuel cells? *J. Electrochem. Soc.* **162**, A2605–A2622 (2015).
11. S. Lu, J. Pan, A. Huang, L. Zhuang, J. Lu, Alkaline polymer electrolyte fuel cells completely free from noble metal catalysts. *Proc. Natl. Acad. Sci. U.S.A.* **105**, 20611–20614 (2018).
12. Y. Yang *et al*., In situ X-ray absorption spectroscopy of a synergistic Co–Mn oxide catalyst for the oxygen reduction reaction. *J. Am. Chem. Soc.* **141**, 1463–1466 (2019).
13. X. Ge *et al*., Oxygen reduction in alkaline media: From mechanisms to recent advances of catalysts. *ACS Catal.* **5**, 4643–4667 (2015).
14. Y. Yang *et al*., Golden palladium zinc ordered intermetallics as oxygen reduction electrocatalysts. *ACS Nano* **13**, 5968–5974 (2019).
15. H. Ren *et al*., Fe/N/C nanotubes with atomic Fe sites: A highly active cathode catalyst for alkaline polymer electrolyte fuel cells. *ACS Catal.* **7**, 6485–6492 (2017).
16. H. T. Chung *et al*., Direct atomic-level insight into the active sites of a high-performance PGM-free ORR catalyst. *Science* **357**, 479–484 (2017).
17. Y. Xiong, Y. Yang, F. J. DiSalvo, H. D. Abruña, Metal–organic-framework-derived Co–Fe bimetallic oxygen reduction electrocatalysts for alkaline fuel cells. *J. Am. Chem. Soc.* **141**, 10744–10750 (2019).
18. J. Suntivich *et al*., Design principles for oxygen-reduction activity on perovskite oxide catalysts for fuel cells and metal-air batteries. *Nat. Chem.* **3**, 546–550 (2011).
19. Q. Zhao, Z. Yan, C. Chen, J. Chen, Spinels: Controlled preparation, oxygen reduction/evolution reaction application, and beyond. *Chem. Rev.* **117**, 10121–10211 (2017).
20. Y. Liang *et al*., Co_3O_4 nanocrystals on graphene as a synergistic catalyst for oxygen reduction reaction. *Nat. Mater.* **10**, 780–786 (2011).
21. Y. Meng *et al*., Structure-property relationship of bifunctional MnO_2 nanostructures: Highly efficient, ultra-stable electrochemical water oxidation and oxygen reduction reaction catalysts identified in alkaline media. *J. Am. Chem. Soc.* **136**, 11452–11464 (2014).
22. Y. Liang *et al*., Covalent hybrid of spinel manganese-cobalt oxide and graphene as advanced oxygen reduction electrocatalysts. *J. Am. Chem. Soc.* **134**, 3517–3523 (2012).
23. C. Li *et al*., Phase and composition controllable synthesis of cobalt manganese spinel nanoparticles towards efficient oxygen electrocatalysis. *Nat. Commun.* **6**, 7345 (2015).
24. C. Wei *et al*., Cations in octahedral sites: A descriptor for oxygen electrocatalysis on transition-metal spinels. *Adv. Mater.* **29**, 1606800 (2017).
25. Y. Yang *et al*., High-loading composition-tolerant Co-Mn spinel oxides with performance beyond 1W/cm^2 in alkaline polymer electrolyte fuel cells. *ACS Energy Lett.* **4**, 1251–1257 (2019).
26. Y. Wang *et al*., Synergistic Mn-Co catalyst outperforms Pt on high-rate oxygen reduction for alkaline polymer electrolyte fuel cells. *Nat. Commun.* **10**, 1506 (2019).
27. A. Indra *et al*., Unification of catalytic water oxidation and oxygen reduction reactions: Amorphous beat crystalline cobalt iron oxides. *J. Am. Chem. Soc.* **136**, 17530–17536 (2014).
28. L. Wan *et al*., Tiny crystalline grain nanocrystal $NiCo_2O_4$/N-doped graphene composite for efficient oxygen reduction reaction. *J. Power Sources* **345**, 41–49 (2017).
29. R. Ning *et al*., Spinel $CuCo_2O_4$ nanoparticles supported on N-doped reduced graphene oxide: A highly active and stable hybrid electrocatalyst for the oxygen reduction reaction. *Langmuir* **29**, 13146–13151 (2013).
30. B. Cao *et al*., Cobalt molybdenum oxynitrides: Synthesis, structural characterization, and catalytic activity for the oxygen reduction reaction. *Angew. Chem. Int. Ed. Engl.* **52**, 10753–10757 (2013).
31. R. D. Shannon, Revised effective ionic radii and systematic studies of interatomic distances in halides and chalcogenides. *Acta Crystallogr. A* **32**, 751–767 (1976).
32. D. P. Shoemaker, J. Li, R. Seshadri, Unraveling atomic positions in an oxide spinel with two Jahn-Teller ions: Local structure investigation of $CuMn_2O_4$. *J. Am. Chem. Soc.* **131**, 11450–11457 (2009).
33. R. E. Davis, G. L. Horvath, C. W. Tobias, The solubility and diffusion coefficient of oxygen in potassium hydroxide solutions. *Electrochim. Acta* **12**, 287–297 (1967).
34. U. A. Paulus, T. J. Schmidt, H. A. Gasteiger, R. J. Behm, Oxygen reduction on a high-surface area Pt/Vulcan carbon catalyst: A thin-film rotating ring-disk electrode study. *J. Electroanal. Chem.* **495**, 134–145 (2001).
35. A. Bonakdarpour *et al*., Impact of loading in RRDE experiments on Fe–N–C catalysts: Two- or four-electron oxygen reduction? *Electrochem. Solid-State Lett.* **11**, B105–B108 (2018).
36. F. Jaouen, J. P. Dodelet, O_2 reduction mechanism on non-noble metal catalysts for PEM fuel cells. Part I: Experimental rates of O_2 electroreduction, H_2O_2 electroreduction, and H_2O_2 disproportionation. *J. Phys. Chem. C* **113**, 15422–15432 (2009).
37. G. Zhang, Q. Wei, X. Yang, A. Tavares, S. Sun, RRDE experiments on noble-metal and noble-metal-free catalysts: Impact of loading on the activity and selectivity of oxygen reduction reaction in alkaline solution. *Appl. Catal. B* **206**, 115–126 (2017).
38. S. Rojas-Carbonell *et al*., Effect of pH on the activity of platinum group metal-free catalysts in oxygen reduction reaction. *ACS Catal.* **8**, 3041–3053 (2018).
39. Y. Li *et al*., Enhancing electrocatalytic performance of bifunctional cobalt-manganese-oxynitride nanocatalysts on graphene. *ChemSusChem* **10**, 68–73 (2017).
40. E. Padgett *et al*., Connecting fuel cell catalyst nanostructure and accessibility using quantitative cryo-STEM tomography. *J. Electrochem. Soc.* **165**, F173–F180 (2018).
41. D. Wang *et al*., Tuning oxygen reduction reaction activity via controllable dealloying: A model study of ordered Cu_3Pt/C intermetallic nanocatalysts. *Nano Lett.* **12**, 5230–5238 (2012).
42. D. B. Williams, C. B. Carter, *Transmission Electron Microscopy: A Textbook for Materials Science* (Springer, New York, ed. 2, 2009), pp. 741.
43. L. A. J. Garvie, A. J. Craven, High-resolution parallel electron energy-loss spectroscopy of Mn $L_{2,3}$-edges in inorganic manganese compounds. *Phys. Chem. Miner.* **21**, 191–206 (1994).
44. F. M. de Groot, J. C. Fuggle, B. T. Thole, G. A. Sawatzky, 2p x-ray absorption of 3d transition-metal compounds: An atomic multiplet description including the crystal field. *Phys. Rev. B Condens. Matter* **42**, 5459–5468 (1990).
45. F. M. F. de Groot, M. Grioni, J. C. Fuggle, J. Ghijsen, G. A. Sawatzky, H. Petersen, Oxygen 1s x-ray-absorption edges of transition-metal oxides. *Phys. Rev. B Condens. Matter* **40**, 5715–5723 (1989).

Downloaded at Cornell University Library on November 21, 2019